Structure of coupled plasmon-phonon modes in degenerate polar semiconductors

1991 J. Phys.: Condens. Matter 3 4825

(http://iopscience.iop.org/0953-8984/3/26/006)

J. Phys.: Condens. Matter 3 (1991) 4825–4840. Printed in the UK

Structure of coupled plasmon–phonon modes in degenerate polar semiconductors

Takeshi Inaoka
Department of Mathematics, Faculty of Engineering, Iwate University, 4-3-5 Ueda, Morioka 020, Japan

Received 6 November 1990, in final form 4 February 1991

Abstract. We investigate the structure of coupled plasmon–phonon modes in degenerate polar semiconductors by decomposing the induced charge density into a component due to carrier density fluctuation and a component resulting from optical phonon polarization. This decomposition of the induced charge density into two components reveals the nature of plasmon–polar phonon coupling. Each energy dispersion branch has its own characteristic mode structure. Analysis of the mode structure with change of carrier concentration shows how the character of the mode structure varies when strong plasmon–polar phonon mixing occurs and, consequently, how the plasmon–phonon coupling transforms its character when strong mixing occurs.

1. Introduction

In doped polar semiconductors, plasmons due to free carriers are coupled with optical phonons when the doping level is appropriately chosen and these excitations lie in the same energy regime. Experimentally, the coupled plasmon–phonon modes have been observed by infrared reflection measurements and Raman scattering measurements (Richter 1984, Abstreiter *et al* 1984 and references therein). Especially, by varying the incident laser frequency, Raman scattering measurements can observe excitation modes of finite q values in a large q region that extends to the single-particle excitation continuum. The principal theoretical approaches to the description of the response of free carriers are the hydrodynamic theory, the Lindhard theory (Lindhard 1954) and the Lindhard–Mermin theory (Mermin 1970). In order to investigate coupled plasmon–phonon modes, these treatments of carriers are combined with the Lorentzian oscillator model, which describes the optical phonon polarization (Richter 1984, Abstreiter *et al* 1984 and references therein). The Lindhard approach (Katayama *et al* 1975, Lemmens and Devreese 1974, Lemmens *et al* 1975, Yuasa *et al* 1986) and the Lindhard–Mermin approach (Abstreiter *et al* 1979) describe the response of free carriers in the random-phase approximation, and involves single-particle excitations in an appropriate manner. The Lindhard approach does not include the effect of collision damping due to impurities, etc. Mermin incorporated the effect of collision damping into the Lindhard theory within the relaxation time approximation (Mermin 1970). This is the Lindhard–Mermin theory. The relaxation time introduced in the Lindhard–Mermin theory is mostly treated as a variable parameter to fit experimental data. These theoretical approaches have been successfully applied to analysis of experimental data, particularly

0953-8984/91/264825 + 16 $03.50

Raman scattering measurements. The central subject of these theoretical analyses was to calculate the energy-loss function, and ultimately, Raman spectra. The energy-loss function plays a central role in describing the Raman scattering cross section (see, for example, equation (75) in Richter (1984) or equation (2.96) in Abstreiter *et al* (1984)).

The present work attempts to gain a deeper insight into the plasmon–polar phonon coupling itself. We investigate the structure of coupled plasmon–polar phonon modes by decomposing the induced charge density of each excitation mode into a component due to carrier density fluctuation and that arising from optical phonon polarization. This decomposition of the induced charge density into two components reveals the nature of plasmon–polar phonon coupling. In addition, we also examine the contribution of each component to the resonance intensity of the energy-loss function. Analysis of the mode structure with change of carrier concentration shows how the character of the mode structure varies when strong plasmon–phonon mixing occurs and, accordingly, how the plasmon–phonon coupling transforms its character when strong mixing occurs.

We are concerned with n-type degenerate polar semiconductors. In doped polar semiconductors such as n-type GaAs and n-type InSb (in particular, in n-type InSb), carrier electrons readily become degenerate as doping becomes heavier, because combination of an exceedingly small effective mass and a large dielectric constant gives a very large effective Bohr radius and, consequently, a very small effective electron density parameter. We adopt n-type InSb as an example for calculation. Our analysis is, for the most part, based on the Lindhard theory (Lindhard 1954) combined with the Lorentzian oscillator model, and only in the last section do we invoke the Lindhard–Mermin theory (Mermin 1970) to explore the effect of collision damping due to impurities, etc. The effect of collision damping makes no significant alteration to the result that has been obtained by the Lindhard approach.

2. Model

We employ the Lindhard theory (and the Lindhard–Mermin theory only in the last section) to describe the response of carriers and the Lorentzian oscillator model to describe the phonon polarization.

The external charge density $s(q, \omega)$, which is introduced to exert perturbation on the system, generates the external potential

$$U(q, \omega) = (4\pi/q^2)s(q, \omega) \tag{1}$$

where q and ω denote a wavevector and an angular frequency, respectively. The total potential $V(q, \omega)$ is produced by both external charges and induced charges:

$$V(q, \omega) = (4\pi/\varepsilon_\infty q^2)[s(q, \omega) + \delta\rho(q, \omega)]. \tag{2}$$

Here ε_∞ is the high-frequency dielectric constant to describe the background screening, and $\delta\rho(q, \omega)$ is the induced charge density. The induced charge density $\delta\rho(q, \omega)$ can be decomposed into a component arising from carrier electron density fluctuation, $\delta\rho_{el}(q, \omega)$, and a component due to phonon polarization, $\delta\rho_{ph}(q, \omega)$:

$$\delta\rho(q, \omega) = \delta\rho_{el}(q, \omega) + \delta\rho_{ph}(q, \omega). \tag{3}$$

The response of carrier electrons is described by the equation

$$\delta\rho_{el}(q, \omega) = e^2\chi(q, \omega)V(q, \omega). \tag{4}$$

In the Lindhard theory, the susceptibility $\chi(q, \omega)$ takes the form

$$\chi(q, \omega) = 2\int \frac{d^3k}{(2\pi)^3} \frac{f(k+q) - f(k)}{\varepsilon(k+q) - \varepsilon(k) + \hbar\omega + i\eta}. \tag{5}$$

In this equation $\varepsilon(k)$ is the energy dispersion of the conduction band, which is given by

$$\varepsilon(k) = \hbar^2 k^2/2m^* \tag{6}$$

η is an infinitesimal positive constant and $f(k)$ is the Fermi–Dirac distribution function for conduction electron states. For simplicity of calculation, we neglect the temperature effect around the Fermi level. In this approximation, $f(k)$ becomes a step function, and the integration on the right-hand side of equation (5) can be performed analytically (Lindhard 1954). The optical phonon polarization $\boldsymbol{P}(\boldsymbol{r}, \omega)$ is described by the equation

$$(\omega_{\mathrm{TO}}^2 - \omega^2 - \mathrm{i}\gamma\omega)\boldsymbol{P}(\boldsymbol{r}, \omega) = -(\varepsilon_\infty/4\pi)\omega_{\mathrm{ph}}^2 \operatorname{grad} V(\boldsymbol{r}, \omega) \tag{7}$$

where ω_{ph} is defined by

$$\omega_{\mathrm{ph}}^2 = [(\varepsilon_0 - \varepsilon_\infty)/\varepsilon_\infty]\omega_{\mathrm{TO}}^2. \tag{8}$$

In equations (7) and (8), ω_{TO} is the transverse optical phonon frequency, ε_∞ and ε_0 are the high-frequency and static dielectric constants at zero carrier concentration, respectively, and γ is the phonon relaxation rate constant. The induced charge density arising from phonon polarization, $\delta\rho_{\mathrm{ph}}(\boldsymbol{r}, \omega)$, is given by

$$\delta\rho_{\mathrm{ph}}(\boldsymbol{r}, \omega) = -\operatorname{div} \boldsymbol{P}(\boldsymbol{r}, \omega). \tag{9}$$

Taking the divergence and Fourier transform of equation (7) yields

$$\delta\rho_{\mathrm{ph}}(\boldsymbol{q}, \omega) = -\frac{\varepsilon_\infty}{4\pi}\frac{\omega_{\mathrm{ph}}^2}{\omega_{\mathrm{TO}}^2 - \omega^2 - \mathrm{i}\gamma\omega} q^2 V(\boldsymbol{q}, \omega). \tag{10}$$

Elimination of $s(\boldsymbol{q}, \omega)$, $\delta\rho_{\mathrm{el}}(\boldsymbol{q}, \omega)$ and $\delta\rho_{\mathrm{ph}}(\boldsymbol{q}, \omega)$ from equations (1), (2), (3), (4) and (10) to obtain the relation between $U(\boldsymbol{q}, \omega)$ and $V(\boldsymbol{q}, \omega)$, and the definition of the dielectric function $\varepsilon(\boldsymbol{q}, \omega)$ as

$$V(\boldsymbol{q}, \omega) = U(\boldsymbol{q}, \omega)/\varepsilon(\boldsymbol{q}, \omega) \tag{11}$$

leads to the dielectric function of the well known form

$$\varepsilon(\boldsymbol{q}, \omega) = \varepsilon_{\mathrm{ph}}(\omega) - (4\pi e^2/q^2)\chi(\boldsymbol{q}, \omega) \tag{12}$$

where $\varepsilon_{\mathrm{ph}}(\omega)$ is the dielectric function to describe the phonon polarization and the background polarization:

$$\varepsilon_{\mathrm{ph}}(\omega) = \varepsilon_\infty\left(1 + \frac{\omega_{\mathrm{ph}}^2}{\omega_{\mathrm{TO}}^2 - \omega^2 - \mathrm{i}\gamma\omega}\right). \tag{13}$$

From equations (1), (4), (10), (11), (12) and (13), $\delta\rho_{\mathrm{el}}(\boldsymbol{q}, \omega)/s(\boldsymbol{q}, \omega)$ and $\delta\rho_{\mathrm{ph}}(\boldsymbol{q}, \omega)/s(\boldsymbol{q}, \omega)$ are expressed as

$$\delta\rho_{\mathrm{el}}(\boldsymbol{q}, \omega)/s(\boldsymbol{q}, \omega) = -[\varepsilon(\boldsymbol{q}, \omega) - \varepsilon_{\mathrm{ph}}(\omega)]/\varepsilon(\boldsymbol{q}, \omega) \tag{14}$$

and

$$\delta\rho_{\mathrm{ph}}(\boldsymbol{q}, \omega)/s(\boldsymbol{q}, \omega) = -[\varepsilon_{\mathrm{ph}}(\omega) - \varepsilon_\infty]/\varepsilon(\boldsymbol{q}, \omega) \tag{15}$$

in terms of $\varepsilon(\boldsymbol{q}, \omega)$, $\varepsilon_{\mathrm{ph}}(\omega)$ and ε_∞. The energy-loss function $F(\boldsymbol{q}, \omega)$, which is defined by

$$F(\boldsymbol{q}, \omega) = \operatorname{Im}[-1/\varepsilon(\boldsymbol{q}, \omega)] \tag{16}$$

plays an important role in examining excitation modes. Here Im denotes the imaginary part. Addition of equations (14) and (15) leads to the alternative expression of the energy-loss function:

$$F(\boldsymbol{q}, \omega) = -\operatorname{Im}\left(\frac{1}{\varepsilon_\infty}\frac{\delta\rho_{\mathrm{el}}(\boldsymbol{q}, \omega)}{s(\boldsymbol{q}, \omega)}\right) - \operatorname{Im}\left(\frac{1}{\varepsilon_\infty}\frac{\delta\rho_{\mathrm{ph}}(\boldsymbol{q}, \omega)}{s(\boldsymbol{q}, \omega)}\right). \tag{17}$$

Table 1. Carrier electron concentrations n and related quantities relevant to the present analysis.

	n (10^{17} cm^{-3})	k_F (10^5 cm^{-1})	m_F^*/m_e	r_0 (Å)	a_B^* (Å)	r_s^*
n_1	0.2717	9.300	0.01591	206.4	594.7	0.3470
n_2	0.5137	11.50	0.01699	166.9	557.0	0.2996
n_3	0.9268	14.00	0.01837	137.1	515.0	0.2662
n_4	1.463	16.30	0.01976	117.7	478.9	0.2458
n_5	2.280	18.90	0.02142	101.5	441.8	0.2298
n_6	3.796	22.40	0.02377	85.68	398.1	0.2152

n_i = Label to indicate each carrier electron concentration.
m_F^*/m_e = Electron-effective mass ratio defined at Fermi wavenumber k_F.
r_0 = Radius of sphere containing one electron $(4\pi r_0^3/3)n = 1$.
a_B^* = Effective Bohr radius $a_B^* = \varepsilon_0\hbar^2/m_F^* e^2$.
r_s^* = Effective electron density parameter $r_s^* = r_0/a_B^*$.

This expression signifies that the value of the energy-loss function can be decomposed into an electron contribution and a phonon contribution. A plot of $\delta\rho_{el}(q, \omega)/[\varepsilon_\infty s(q, \omega)]$, $\delta\rho_{ph}(q, \omega)/[\varepsilon_\infty s(q, \omega)]$ and $1/\varepsilon(q, \omega)$ $(= V(q, \omega)/U(q, \omega))$ on the complex plane for each resonance mode elucidates the structure of the coupled plasmon–polar phonon mode and the contribution of the carrier electron gas or the phonon polarization to the energy loss. As is seen from equations (16) and (17), the sum of $\mathrm{Im}[\delta\rho_{el}(q, \omega)/\varepsilon_\infty s(q, \omega)]$ and $\mathrm{Im}[\delta\rho_{ph}(q, \omega)/\varepsilon_\infty s(q, \omega)]$ is equal to $\mathrm{Im}[1/\varepsilon(q, \omega)]$. We take n-type InSb as an example for calculation. The conduction band dispersion of InSb, though almost isotropic, is highly non-parabolic (see Kane (1957) or figure 2 in Inaoka *et al* (1987)). This effect of non-parabolicity is incorporated into the calculation by using the effective mass defined at the Fermi wavenumber k_F by

$$\frac{1}{m_F^*} = \frac{1}{\hbar^2 k_F}\left(\frac{dE(k)}{dk}\right)_{k=k_F}. \tag{18}$$

This is a good approximation when we are concerned with excitation modes whose wavenumbers q are small compared with k_F. The conduction band dispersion $E(k)$ can be calculated by Kane's scheme (equation (10) in Kane (1957)) with the band parameter values (Isaacson 1968), $m_0^*/m_e = 0.0136$ (conventional effective-mass ratio defined at the conduction band bottom), $\Delta = 0.98$ eV (spin–orbit splitting) and $E_g = 0.235$ eV (band gap for $T = 1.4$ K). The above effective mass m_F^* is employed as the effective mass m^* in the Lindhard susceptibility $\chi(q, \omega)$. Incidentally, the band gap E_g has an appreciable temperature dependence. At $T = 290$ K, the band gap takes the value $E_g = 0.17$ eV (Roberts and Quarrington 1955), which leads to a somewhat different value of m_F^*. In the following calculation, we use the values of ε_∞, ε_0, ω_{TO} and γ that were determined by Hass and Henvis (1962) by means of infrared reflection measurements.

3. Variation of the mode structure in strong plasmon–polar phonon mixing

Plasmon energies vary with change of doping level, namely change of carrier concentration, and strong plasmon–polar phonon mixing occurs when plasmon energies cross over phonon energies. In this section, we explore how the mode structure varies when strong mixing takes place. In table 1, values of the effective carrier electron density

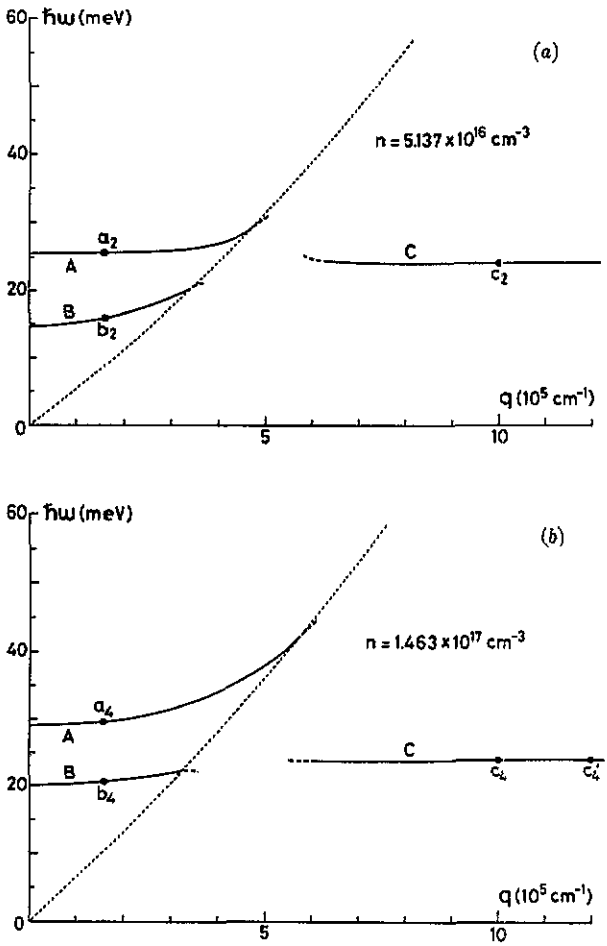

Figure 1. Energy dispersion diagrams for two carrier concentrations (n_2 and n_4 in table 1). The dotted and broken curves are described in the text.

parameter r_s^* are presented for six carrier concentrations, which cover the strong mixing concentration regime. In view of these high effective densities, we can expect carrier electrons to be highly degenerate in the carrier concentration regime where strong plasmon–phonon mixing occurs.

We can draw energy dispersion curves by calculating the energy-loss function $F(q, \omega)$ and locating resonance modes. Figure 1 exhibits the energy dispersion diagrams for two carrier concentrations (n_2 and n_4 in table 1). In each panel, the electron–hole pair excitation continuum extends on the right side of the dotted curve, and the resonance intensity of the energy-loss function decays away on the broken curves. There exist three dispersion branches, which we name A, B and C, as shown in each panel. The mode on branch A or B immediately decays away when it enters the pair excitation continuum. With decreasing q the mode on branch C gradually loses its resonance intensity and disappears into the background intensity due to pair excitations. In figures 6 and 18 of Richter (1984), the existence of the three dispersion branches is shown as a three-dimensional view of the q and ω dependences of the energy-loss function. As carrier concentration decreases from above to below the strong mixing concentration regime,

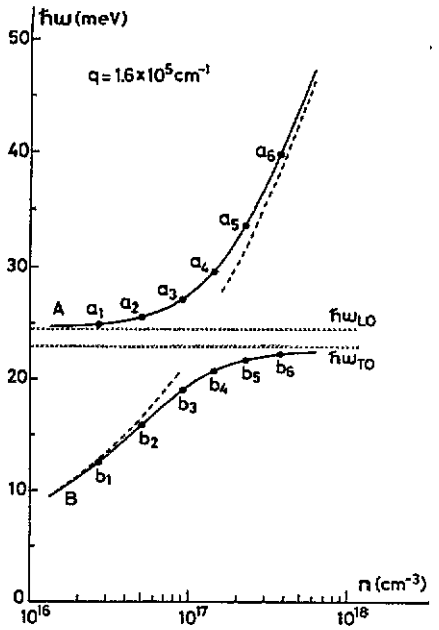

Figure 2. Carrier concentration dependence of energies of the two resonance modes at $q = 1.6 \times 10^5\ \mathrm{cm}^{-1}$. The modes a_2, a_4 and b_2, b_4 are exhibited in figure 1. The two broken curves are described in the text.

the upper branch A hangs down to the phonon energy regime (though this branch always lies above the longitudinal optical phonon energy $\hbar\omega_{LO} = 24.45$ meV), which repels the lower branch B to a lower energy range.

Figure 2 exhibits the carrier concentration dependence of energies of the two modes at $q = 1.6 \times 10^5\ \mathrm{cm}^{-1}$. The abscissa is indicated in logarithmic scale. The subscripts 1 to 6 of mode labels signify carrier concentrations and correspond to the same subscripts of n in table 1. The energy of the higher-energy mode approaches the longitudinal optical phonon energy $\hbar\omega_{LO}$ (=24.45 meV) with decrease of carrier concentration, and the energy of the lower-energy mode approaches the transverse optical phonon energy $\hbar\omega_{TO}$ (=22.90 meV) with increase of carrier concentration. The broken curve in the higher concentration range represents the plasmon energy that is obtained by setting $\varepsilon_{ph}(\omega)$ in equation (13) equal to ε_∞; and the broken curve in the lower concentration range indicates the plasmon energy that is obtained by setting $\varepsilon_{ph}(\omega)$ in equation (13) equal to ε_0. This carrier concentration dependence of the two mode energies asserts that strong plasmon–phonon mixing takes place in a concentration range $n \sim 10^{17}\ \mathrm{cm}^{-3}$.

We investigate how the mode structure varies when strong mixing occurs. Figure 3 exhibits the structure of the two resonance modes at $q = 1.6 \times 10^5\ \mathrm{cm}^{-1}$ for various carrier concentrations. Here $\delta\rho_{el}(q, \omega)/[\varepsilon_\infty s(q, \omega)]$, $\delta\rho_{ph}(q, \omega)/[\varepsilon_\infty s(q, \omega)]$ and $1/\varepsilon(q, \omega)$ $(= V(q, \omega)/U(q, \omega))$ are plotted on the complex plane as full squares, full triangles and open circles, respectively. Each of these modes corresponds to one of the modes in figure 2, according to mode labelling. The panels (*a*) and (*b*) of figure 3 show the structure of higher- and lower-energy resonance modes, respectively. The value of $1/\varepsilon(q, \omega)$ becomes pure imaginary or almost pure imaginary at resonance (see open circles in figure 3) because resonance corresponds to the pole of $1/\varepsilon(q, \omega)$. The imaginary part of $1/\varepsilon(q, \omega)$ gives the opposite sign of the value of the energy-loss function. It is

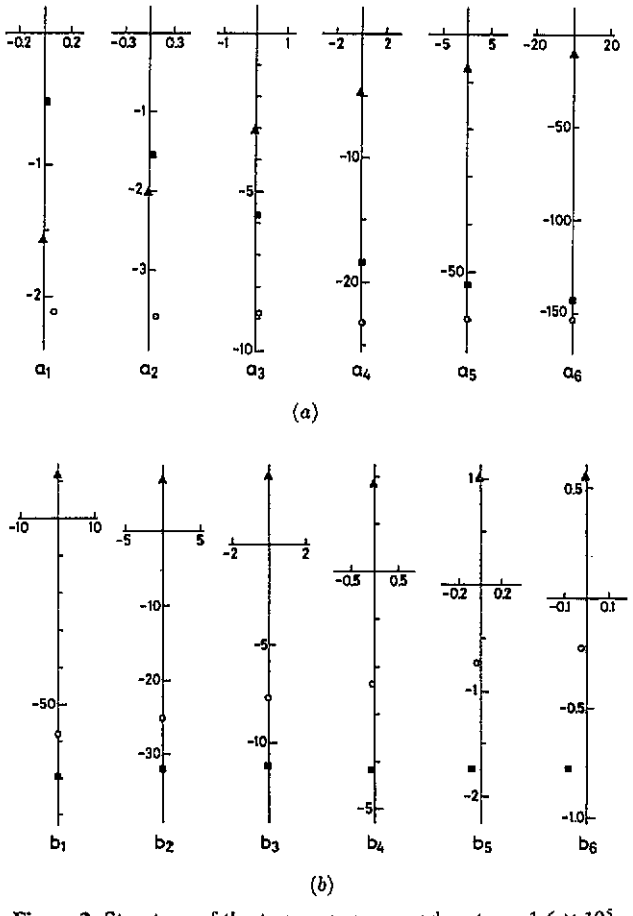

Figure 3. Structure of the two resonance modes at $q = 1.6 \times 10^5$ cm^{-1} for six carrier concentrations listed in table 1: (*a*) higher-energy modes; (*b*) lower-energy modes (see figure 2). For each mode, the symbols used are: (■) $\delta\rho_{el}(q, \omega)/[\varepsilon_\infty s(q, \omega)]$; (▲) $\delta\rho_{ph}(q, \omega)/[\varepsilon_\infty s(q, \omega)]$; (○) $1/\varepsilon(q, \omega)$ $(= V(q, \omega)/U(q, \omega))$. The abscissa and the ordinate are the real and imaginary axes, respectively.

important to note that $s(q, \omega)$ has the same phase as $U(q, \omega)$ (see equation (1)) when we consider the phase relation between $\delta\rho_{el}(q, \omega)$ and $V(q, \omega)$ or between $\delta\rho_{ph}(q, \omega)$ and $V(q, \omega)$. As is seen from equation (17), the imaginary parts of $-\delta\rho_{el}(q, \omega)/[\varepsilon_\infty s(q, \omega)]$ and $-\delta\rho_{ph}(q, \omega)/[\varepsilon_\infty s(q, \omega)]$ make an additive contribution to the value of the energy-loss function. What is common to all the modes in figure 3 is that $\delta\rho_{el}(q, \omega)$ has completely the same phase as $V(q, \omega)$ because these modes exist outside the pair excitation continuum and $\chi(q, \omega)$ is real and positive (see equation (4)).

First, we analyse the structure of higher-energy modes, which is shown in figure 3(*a*). What is characteristic of higher-energy modes is that $\delta\rho_{el}(q, \omega)$ has the same or almost the same phase as $\delta\rho_{ph}(q, \omega)$. This is the mode character of branch A. Both the response of carriers and the phonon polarization operate to enhance the energy-loss intensity, because $\mathrm{Im}[\delta\rho_{el}(q, \omega)/\varepsilon_\infty s(q, \omega)]$ and $\mathrm{Im}[\delta\rho_{ph}(q, \omega)/\varepsilon_\infty s(q, \omega)]$ are both negative. The amplitude ratio of $\delta\rho_{el}(q, \omega)$ and $\delta\rho_{ph}(q, \omega)$ varies significantly with change of carrier concentration. Above the strong mixing concentration regime, the amplitude of $\delta\rho_{el}(q, \omega)$ is considerably larger than that of $\delta\rho_{ph}(q, \omega)$, which implies that the mode is

plasmon-like. With decrease of carrier concentration, however, $\delta\rho_{ph}(q, \omega)$ becomes more and more influential, and below the strong mixing concentration regime, $\delta\rho_{ph}(q, \omega)$ acquires a larger amplitude. This variation in structure with decrease of carrier concentration implies the transformation from plasmon-like to phonon-like nature.

Next, we turn our attention to the structure of lower-energy modes, which is shown in figure 3(*b*). The feature in the structure of lower-energy modes is that $\delta\rho_{el}(q, \omega)$ is in anti-phase relation with $\delta\rho_{ph}(q, \omega)$, and that the amplitude of $\delta\rho_{el}(q, \omega)$ is always larger than that of $\delta\rho_{ph}(q, \omega)$. This is the mode character of branch B. Carrier electrons make a dominant contribution to the energy loss, and the phonon polarization acts to reduce the energy loss because the imaginary part of $\delta\rho_{ph}(q, \omega)/[\varepsilon_\infty s(q, \omega)]$ is positive. The amplitude ratio of $\delta\rho_{el}(q, \omega)$ and $\delta\rho_{ph}(q, \omega)$ varies conspicuously with change of carrier concentration, though the amplitude of $\delta\rho_{el}(q, \omega)$ is larger than that of $\delta\rho_{ph}(q, \omega)$ over the whole range of carrier concentration. Above the strong mixing concentration regime, the amplitude of $\delta\rho_{el}(q, \omega)$ is, in large part, cancelled by that of $\delta\rho_{ph}(q, \omega)$. With decrease of carrier concentration, $\delta\rho_{el}(q, \omega)$ becomes more and more predominant over $\delta\rho_{ph}(q, \omega)$, and below the strong mixing concentration regime the lower-energy mode becomes plasmon-like.

As is stated in section 1, the present analysis is based on the Lindhard approach, which does not include the effect of collision damping due to impurities, etc. In this approach, the energy width of the plasmon resonance peak of the energy-loss function originates only from coupling with the phonon whose damping is taken into account by the relaxation rate constant γ (see equation (13)). Accordingly, as the mode becomes more plasmon-like, the resonance peak becomes sharper. This is the reason why $\delta\rho_{el}(q, \omega)/[\varepsilon_\infty s(q, \omega)]$, $\delta\rho_{ph}(q, \omega)/[\varepsilon_\infty s(q, \omega)]$ and $1/\varepsilon(q, \omega)$ $(= V(q, \omega)/U(q, \omega))$ have very large imaginary parts in modes a_6, a_5 or b_1, b_2.

Here we examine the integrated resonance intensity, namely, the integrated area of the resonance peak of the energy-loss function, which is defined by

$$I = \int_{\text{peak}} \text{Im}\left(\frac{-1}{\varepsilon(q, \omega)}\right) \text{d}(\hbar\omega). \tag{19}$$

This quantity plays a significant role in analysing the intensity in the excitation energy spectrum. According to equations (16) and (17), the integrated resonance intensity I can be decomposed into an electron component and a phonon component:

$$I = I_{el} + I_{ph} \tag{20}$$

where I_{el} and I_{ph} are expressed as

$$I_{el} = -\int_{\text{peak}} \text{Im}\left(\frac{1}{\varepsilon_\infty}\frac{\delta\rho_{el}(q, \omega)}{s(q, \omega)}\right) \text{d}(\hbar\omega) \tag{21}$$

and

$$I_{ph} = -\int_{\text{peak}} \text{Im}\left(\frac{1}{\varepsilon_\infty}\frac{\delta\rho_{ph}(q, \omega)}{s(q, \omega)}\right) \text{d}(\hbar\omega) \tag{22}$$

respectively. Figure 4 shows the carrier concentration dependence of the integrated resonance intensity of the two resonance modes at $q = 1.6 \times 10^5$ cm^{-1}. The curves A and B in figure 4, which correspond to the curves A and B in figure 2, indicate the resonance intensity of the higher- and lower-energy modes at $q = 1.6 \times 10^5$ cm^{-1},

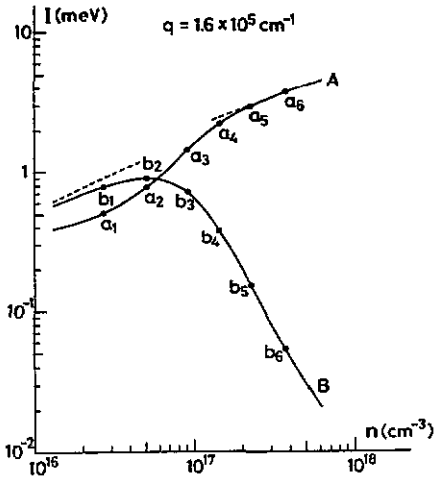

Figure 4. Carrier concentration dependence of the integrated resonance intensity I of the two modes at $q = 1.6 \times 10^5$ cm^{-1}: curve A, higher-energy mode; curve B, lower-energy mode. The two broken curves are described in the text. The ordinate and the abscissa are both indicated in logarithmic scale.

respectively. The broken curve describing the asymptotic behaviour of curve A corresponds to the broken curve in the higher concentration range in figure 2, and it represents the plasmon resonance intensity that is obtained by setting $\varepsilon_{ph}(\omega)$ equal to ε_∞ (see equation (13)). Similarly, the broken curve describing the asymptotic behaviour of curve B corresponds to the broken curve in the lower concentration range in figure 2, and it represents the plasmon resonance intensity that is obtained by setting $\varepsilon_{ph}(\omega)$ equal to ε_0. Here we follow each curve from higher to lower carrier concentration, considering the corresponding variation of the mode structure presented in figure 3.

The higher-energy mode (curve A) is plasmon-like above the strong mixing concentration regime, as shown by the mode structure in figure 3(*a*) and by the asymptotic behaviour of the resonance intensity in figure 4 (note the broken curve in the higher concentration range). With decrease of carrier concentration, the resonance intensity of the higher-energy mode decreases monotonically and more quickly in the strong mixing concentration regime. Below the strong mixing concentration regime, the higher-energy mode becomes phonon-like, as is shown by the mode structure in figure 3(*a*). With further decrease of carrier concentration, the resonance intensity decreases more and more slowly and approaches the resonance intensity of the longitudinal optical phonon in the absence of carrier electrons ($\approx$0.30). Figure 5(*a*) exhibits the carrier concentration dependence of I_{el}/I and I_{ph}/I for the higher-energy mode. This clarifies the transformation from plasmon-like to phonon-like nature with decrease of carrier concentration.

Above the strong mixing concentration regime, the lower-energy mode involves considerable cancellation between $\delta\rho_{el}(q, \omega)$ and $\delta\rho_{ph}(q, \omega)$, as shown in figure 3(*b*), and this mode has very weak resonance intensity (curve B in figure 4). As the upper dispersion branch hangs down on the lower dispersion branch with decrease of carrier concentration, the lower-energy mode becomes coupled with the higher-energy mode more strongly and gains stronger resonance intensity. On passing through the strong mixing concentration regime, however, the resonance intensity I turns from acclivity to declivity. Below the strong mixing concentration regime, the mode becomes plasmon-like, as is shown by the mode structure in figure 3(*b*), and with decrease of carrier

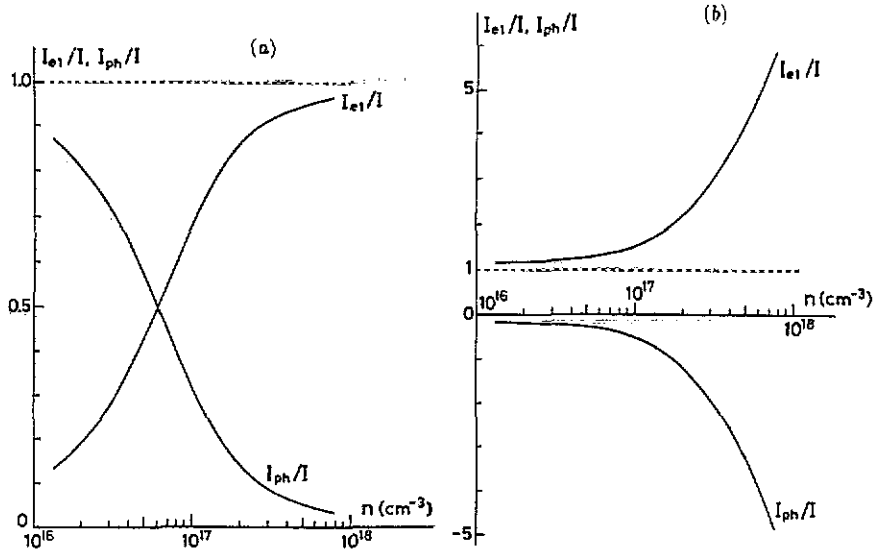

Figure 5. Carrier concentration dependence of I_{el}/I and I_{ph}/I of the two resonance modes at $q = 1.6 \times 10^5$ cm^{-1}: (*a*) higher-energy mode; (*b*) lower-energy mode.

concentration the mode declines in resonance intensity in accordance with its plasmon nature. Figure 5(*b*) displays the carrier concentration dependence of I_{el}/I and I_{ph}/I for the lower-energy mode. In the lower-energy mode, I_{ph} is negative, because the phonon polarization acts against carrier electrons to suppress the resonance intensity. Above the strong mixing concentration regime, the value of I_{el} is very close to the absolute value of I_{ph}. This corresponds to the fact that, as is shown in figure 3(*b*), $\delta\rho_{el}(q, \omega)$ and $\delta\rho_{ph}(q, \omega)$ almost cancel each other, though $\delta\rho_{el}(q, \omega)$ survives. With decrease of carrier concentration, the value of I_{el}/I decreases and approaches unity, which implies that the mode becomes plasmon-like.

Next, we explore the variation in mode structure of branch C with change of carrier concentration. Figure 6 exhibits the mode structure of the resonance mode at $q = 10 \times 10^5$ cm^{-1} for various carrier concentrations. The subscripts in mode labels indicate carrier concentrations in accordance with the subscripts of n in table 1. What is characteristic of these modes is that $\delta\rho_{ph}(q, \omega)$, which has almost the same phase as $V(q, \omega)$, has a larger amplitude than $\delta\rho_{el}(q, \omega)$ and that $\delta\rho_{el}(q, \omega)/[\varepsilon_\infty s(q, \omega)]$ has a positive imaginary part, which acts to suppress the energy loss. These characteristics imply that the phonon polarization plays the leading role and that carrier electrons have a screening effect on phonon polarization. In each of these modes, $\delta\rho_{el}(q, \omega)/[\varepsilon_\infty s(q, \omega)]$ has a finite real part, because the susceptibility $\chi(q, \omega)$ has a finite imaginary part owing to pair excitations (see equation (4)). With decreasing carrier concentration the imaginary part of $\delta\rho_{ph}(q, \omega)/[\varepsilon_\infty s(q, \omega)]$, which is negative, gains a larger absolute value and the imaginary part of $\delta\rho_{el}(q, \omega)/[\varepsilon_\infty s(q, \omega)]$, which is positive, becomes smaller. In addition, with decrease of carrier concentration the resonance peak of the energy-loss function acquires stronger intensity I and its energy gradually approaches the longitudinal optical phonon energy $\hbar\omega_{LO}$. These features assert that with decrease of carrier concentration the screening effect of carrier electrons on phonon polarization works less and less effectively and finally the partially screened phonon mode reduces to the longitudinal optical phonon mode, which arises in the absence of carrier electrons.

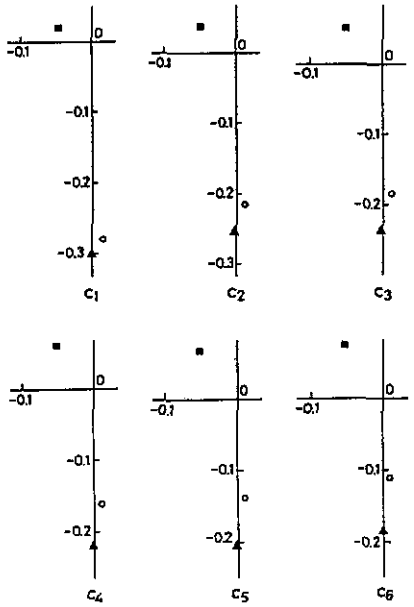

Figure 6. Structure of the resonance mode at $q = 10 \times 10^5\ \mathrm{cm}^{-1}$ for six carrier concentrations listed in table 1. The modes c_2 and c_4 are exhibited in figure 1. For each mode, the symbols used are: (■) $\delta\rho_{\mathrm{el}}(q,\omega)/[\varepsilon_\infty s(q,\omega)]$; (▲) $\delta\rho_{\mathrm{ph}}(q,\omega)/[\varepsilon_\infty s(q,\omega)]$; (○) $1/\varepsilon(q,\omega)$ $(=V(q,\omega)/U(q,\omega))$.

4. Variation of the mode structure with change of wavenumber q

In this section we examine the variation of the mode structure along each dispersion branch, namely, with change of wavenumber q. The mode structure of branch A and that of branch B are characterized by the coherent phase relation and the anti-phase relation of $\delta\rho_{\mathrm{el}}(q,\omega)$ and $\delta\rho_{\mathrm{ph}}(q,\omega)$, respectively. Figure 7 shows the q dependence of I and figure 8 exhibits the q dependence of I_{el}/I and I_{ph}/I along each of the branches A and B. Carrier concentrations are indicated by the same subscripts of n as in table 1. Each curve in figures 7 or 8 terminates at a finite q just before going into the electron–hole pair excitation continuum. The resonance intensity of the mode on branch A or B immediately decays away into the background intensity due to pair excitations when the mode enters the pair excitation continuum.

First, we focus our attention on the case of the highest carrier concentration n_6. The value of I_{el}/I of branch A is close to unity and approaches unity with increase of q (curve n_6 in figure 8(a)). This corresponds to the fact that at this carrier concentration the higher-energy branch A is plasmon-like and that with increase of q the mode on branch A becomes more plasmon-like because its energy becomes higher and gets further apart from the phonon energy regime. Owing to the plasmon nature, with increase of q the resonance intensity I decreases monotonically (curve n_6 in figure 7(a)). As for the branch B, the value of I_{el} is always larger than the absolute value of I_{ph} for each mode on this branch (see figure 8(b)). At this carrier concentration, however, the value of I_{el} is very close to the absolute value of I_{ph}, and the former strikingly gets closer to the latter with increase of q (curves n_6 in figure 8(b)). In addition, at this carrier concentration the resonance intensity I of branch B is very weak, and decreases monotonically with

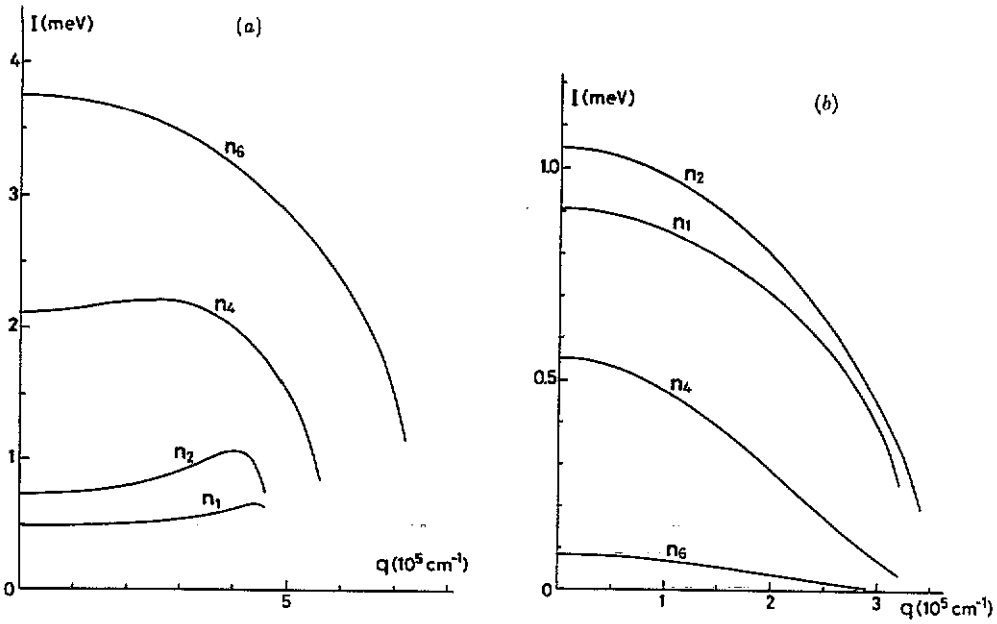

Figure 7. The q dependence of I along each of the two dispersion branches A and B: (a) branch A; (b) branch B. The labels n_1, n_2, n_4 and n_6 indicate carrier concentrations (see table 1).

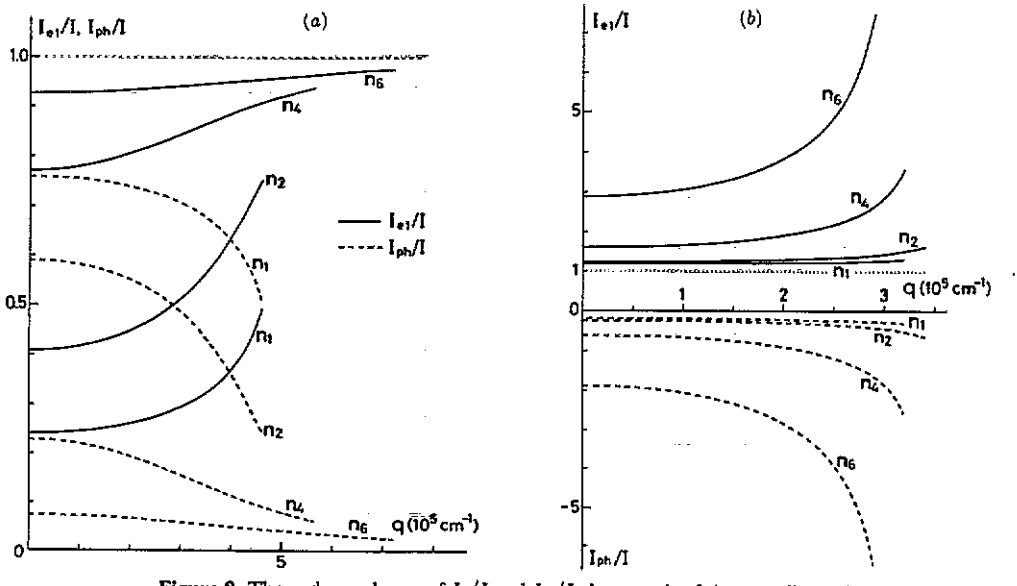

Figure 8. The q dependence of I_{el}/I and I_{ph}/I along each of the two dispersion branches A and B: (a) branch A; (b) branch B. The labels n_1, n_2, n_4 and n_6 indicate carrier concentrations (see table 1).

increase of q (curve n_6 in figure 7(b)). These features imply that the plasmon-like branch A, which lies well above branch B, has quite a weak effect on the modes on branch B, and that with increase of q this effect of the plasmon-like branch A becomes weaker and weaker because the energy of the plasmon-like branch A becomes higher and becomes further apart from the energy of branch B.

Next, we turn our attention to the case of lower carrier concentration n_2. The intensity fraction I_{el}/I of branch B is close to unity throughout the whole range of q, though it shows a slight enhancement with increase of q (full curve n_2 in figure 8(b)). This implies that at this carrier concentration branch B is plasmon-like, though it retains quite a small fraction of phonon character especially in the larger q range. The intensity fraction I_{el}/I or I_{ph}/I of branch A has a significant q dependence (curves n_2 in figure 8(a)). This indicates that, though the phonon character is dominant in the smaller q range, the plasmon character survives persistently in the larger q range. This surviving plasmon character is also reflected in the energy dispersion. As is displayed in figure 1(a), the energy dispersion curve of branch A, which is flat in the smaller q range, bends up significantly in a q range $q \geqslant 4 \times 10^5\,\mathrm{cm}^{-1}$. This upward bending of the energy dispersion curve is attributed to the surviving plasmon character in the larger q range. With increase of q, the mode on branch A acquires more plasmon character and its resonance intensity I increases gradually. However, when the plasmon nature becomes quite predominant and the dispersion curve begins to bend up significantly, the resonance intensity I turns down and decreases (curve n_2 in figure 7(a)). This analysis of branch A indicates that, as the branch A goes down in energy and approaches the phonon energy regime with decrease of carrier concentration, the mode character is transformed from plasmon-like to phonon-like, and that this transformation germinates in the smaller q range, and gradually spreads to the larger q range with decrease of carrier concentration.

The character of variation of I_{el}/I, I_{ph}/I and I at the intermediate carrier concentration n_4 is between the character at the lower concentration n_2 and that at the higher concentration n_6.

As carrier concentration decreases from n_6 to n_2, the resonance intensity I of branch B increases over the whole range of q (see figure 7(b)). However, with further decrease of carrier concentration, the resonance intensity I declines, as is seen from the curve n_1 in figure 7(b). This variation of I corresponds to the carrier concentration dependence of I of the lower-energy mode at $q = 1.6 \times 10^5\,\mathrm{cm}^{-1}$, which is shown by the curve B in figure 4.

Next, we investigate the variation in mode structure of branch C with change of q. Since the situation is the same for every carrier concentration, we present only the result for the carrier concentration n_4. Figure 9 shows the mode structure of resonance modes at various q values. As is stated in the preceding section, the phonon polarization plays the leading role in modes of branch C, and carrier electrons operate to screen the phonon polarization. With increase of q, the imaginary part of $\delta\rho_{ph}(q, \omega)/[\varepsilon_\infty s(q, \omega)]$, which is negative, acquires a larger absolute value, while the imaginary part of $\delta\rho_{el}(q, \omega)/[\varepsilon_\infty s(q, \omega)]$, which is positive, decreases significantly after just a slight enhancement. With increasing q, the mode on branch C gains stronger resonance intensity I of the energy-loss function, and its energy asymptotically approaches the longitudinal optical phonon energy $\hbar\omega_{LO}$. For larger q outside the pair excitation continuum, the resonance intensity saturates to the intensity of the longitudinal optical phonon mode, which arises in the absence of carrier electrons. These features assert that, with increase of q, the screening effect of carrier electrons operates less and less effectively, and that finally the mode on branch C reduces to the longitudinal optical phonon mode in the absence of

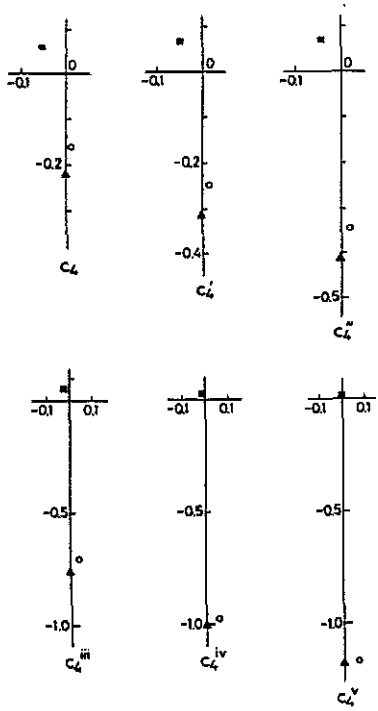

Figure 9. Structure of resonance modes on branch C at various values of q. The labels c_4, c_4', c_4'', c_4^{iii}, c_4^{iv} and c_4^{v} signify the resonance modes at $q = 10, 12, 14, 22, 30$ and $38 \times 10^5\,\mathrm{cm}^{-1}$, respectively. For each mode, the symbols used are: (■) $\delta\rho_{el}(q, \omega)/[\varepsilon_\infty s(q, \omega)]$; (▲) $\delta\rho_{ph}(q, \omega)/[\varepsilon_\infty s(q, \omega)]$; (○) $1/\varepsilon(q, \omega)$ $(= V(q, \omega)/U(q, \omega))$.

carriers. In the resonance mode c_4^{v}, $\delta\rho_{el}(q, \omega)$ has anti-phase relation with $V(q, \omega)$ (and $\delta\rho_{ph}(q, \omega)$), because this mode is outside the pair excitation continuum and the susceptibility $\chi(q, \omega)$ becomes real (see equation (4)).

5. Summary and discussion

There exist three energy dispersion branches, which are named A, B and C, as is displayed in figure 1. The results of the present analysis are summarized as follows:

(i) The mode structure of branch A is characterized by the coherent phase relation of $\delta\rho_{el}(q, \omega)$ and $\delta\rho_{ph}(q, \omega)$. Decrease of carrier concentration induces the transformation of the mode structure from plasmon-like to phonon-like character. Above the strong mixing concentration regime, $|\delta\rho_{el}(q, \omega)|$ is larger than $|\delta\rho_{ph}(q, \omega)|$ (plasmon-like), and below the strong mixing concentration regime, $|\delta\rho_{ph}(q, \omega)|$ is larger than $|\delta\rho_{el}(q, \omega)|$ (phonon-like). This transformation from plasmon-like to phonon-like character begins in the smaller q range, and with decrease of carrier concentration it spreads gradually up to the larger q range. With decrease of carrier concentration, the resonance intensity of branch A declines, and finally it saturates to the resonance intensity of the longitudinal optical phonon in the absence of carriers.

(ii) The mode structure of branch B is characterized by the anti-phase relation of $\delta\rho_{el}(q, \omega)$ and $\delta\rho_{ph}(q, \omega)$. In this case $|\delta\rho_{el}(q, \omega)|$ is larger than $|\delta\rho_{ph}(q, \omega)|$ throughout the whole range of carrier concentration. Above the strong mixing concentration regime,

however, $\delta\rho_{el}(q, \omega)$ is, for the most part, cancelled by $\delta\rho_{ph}(q, \omega)$, and the resonance intensity of this branch is quite weak. With decrease of carrier concentration, $|\delta\rho_{el}(q, \omega)|$ becomes larger compared with $|\delta\rho_{ph}(q, \omega)|$, and the mode character evolves into the plasmon-like character. As the plasmon character becomes more influential with decrease of carrier concentration, the resonance intensity of branch B becomes stronger. However, after the plasmon character is established, the resonance intensity declines with further decrease of carrier concentration, as is consistent with the plasmon nature.

(iii) The mode character of branch C is that $|\delta\rho_{ph}(q, \omega)|$ is larger than $|\delta\rho_{el}(q, \omega)|$. Here $\delta\rho_{ph}(q, \omega)$ and $\delta\rho_{el}(q, \omega)$ are in anti-phase relation outside the electron–hole pair excitation continuum. The mode on branch C is identified as the longitudinal optical phonon mode, which is partially screened by carriers. With increase of q or with decrease of carrier concentration, this screening effect operates less and less effectively, which leads to enhancement of the resonance intensity.

Here we mention the effect of collision damping due to impurities, acoustic phonons, etc. The Lindhard–Mermin theory involves this effect within the relaxation time approximation (Mermin 1970), and gives the electron susceptibility

$$\chi_{LM}(q, \omega) = \frac{[1 + (i/\omega\tau)]\chi(q, \omega + i/\tau)}{1 + (i/\omega\tau)[\chi(q, \omega + i/\tau)/\chi(q, \omega = 0)]} \tag{23}$$

where τ is the relaxation time to describe the effect of collision damping, $\chi(q, \omega = 0)$ is the Lindhard susceptibility for $\omega = 0$ and for an infinitesimal positive constant η (see equation (5)), and $\chi(q, \omega + i/\tau)$ is the Lindhard susceptibility for a finite positive η, namely, for $\eta = \hbar/\tau$. For $T = 0$, the k integration in the Lindhard susceptibility can be performed analytically also for a finite η ($=\hbar/\tau$). The relaxation time τ is mostly treated as a fitting parameter in each analysis of experimental data. This quantity is considered to vary with change of doping level. However, here we calculate the mode structure and the resonance intensity for various carrier concentrations with a few reasonable values of τ, in order to confirm that the effect of collision damping has no essential influence on the above result obtained by the Lindhard approach. We take a few values of τ from a range $\hbar/\tau \leqslant 2$ meV. The value of τ is estimated to be around 1 meV from the effective-mass ratio $m^*/m \simeq 0.02$ and the conduction electron mobility $\mu_e \simeq 50\,000\ \mathrm{cm^2\ s^{-1}\ V^{-1}}$ (see figure 3 in Rollin and Petford (1955)) by virtue of the relation $\mu_e = e\tau/m^*$. In the case of n-type GaAs, the value of $\hbar\tau$ is taken to be about 7–11 meV to achieve good agreement with experimental data (see Abstreiter *et al* (1979) and figure 14 in Richter (1984)). In the case of n-type InSb, however, the value $\hbar/\tau = 1$ or 2 meV is reasonable, in view of the fact that the electron mobility μ_e of InSb is one order of magnitude larger than that of GaAs. What derives from this analysis is that the effect of collision damping broadens the resonance peak in the ω dependence of the energy-loss function, and this broadening is quite remarkable for plasmon-like modes as a_6, a_5 or b_1, b_2, and that this effect has no substantial influence on the mode energy, the integrated resonance intensity of the energy-loss function and the character of the mode structure, namely, the phase relation and the amplitude ratio of $\delta\rho_{el}(q, \omega)$ and $\delta\rho_{ph}(q, \omega)$.

Thus far we have examined the structure of coupled plasmon–polar phonon modes in the *bulk*. However, the present analysis is also helpful to improve the understanding of those modes at the *surface*. We can investigate the structure of coupled plasmon–phonon *surface* modes by the same means of decomposing the induced charge density into a carrier component and a phonon component. We intend to report on this analysis of coupled surface modes in the near future (Inaoka 1991).

Acknowledgments

The author would like to thank M Inaoka for her help with drawing figures. All the numerical calculations in the present work were carried out at the Iwate University Computer Centre.

References

Abstreiter G, Cardona M and Pinczuk A 1984 *Light Scattering in Solids IV* ed M Cardona and G Güntherodt (Berlin: Springer) p 5
Abstreiter G, Trommer R, Cardona M and Pinczuk A 1979 *Solid State Commun.* **30** 703
Hass M and Henvis B W 1962 *J. Phys. Chem. Solids* **23** 1099
Inaoka T 1991 *Surf. Sci.* to be published
Inaoka T, Newns D M and Egdell R G 1987 *Surf. Sci.* **186** 290
Isaacson R A 1968 *Phys. Rev.* **169** 312
Kane E O 1957 *J. Phys. Chem. Solids* **1** 249
Katayama S, Murase K and Kawamura H 1975 *Solid State Commun.* **16** 945
Lemmens L F, Brosens F and Devreese J T 1975 *Solid State Commun.* **17** 337
Lemmens L F and Devreese J T 1974 *Solid State Commun.* **14** 1339
Lindhard J 1954 *K. Danske Vidensk. Selsk. Mat.-Fys. Meddr.* **28** No 8
Mermin N D 1970 *Phys. Rev.* B **1** 2362
Richter W 1984 *Polarons and Excitons in Polar Semiconductors and Ionic Crystals* ed J T Devreese and F Peeters (New York: Plenum) p 209
Roberts V and Quarrington J E 1955 *J. Electron.* **1** 152
Rollin B V and Petford A D 1955 *J. Electron.* **1** 171
Yuasa T, Naritsuka S, Mannoh M, Shinozaki K, Yamanaka K, Nomura Y, Mihara M and Ishii M 1986 *Phys. Rev.* B **33** 1222